Phase transition and domain formation in ferroaxial crystals

T. Hayashida,[1] Y. Uemura,[2] K. Kimura,[1] S. Matsuoka,[2] M. Hagihala,[3,4] S. Hirose,[5] H. Morioka,[6] T. Hasegawa,[2] and T. Kimura[1]

[1]*Department of Advanced Materials Science, University of Tokyo, Kashiwa, Chiba 277–8561, Japan*
[2]*Department of Applied Physics, University of Tokyo, Hongo, Tokyo 113–8656, Japan*
[3]*Institute of Materials Structure Science, High Energy Accelerator Research Organization (KEK), Tokai, Ibaraki 319–1106, Japan*
[4]*Materials Science Research Center, Japan Atomic Energy Agency, Tokai, Ibaraki 319–1195, Japan*
[5]*Murata Manufacturing Co., Ltd., Nagaokakyo–shi, Kyoto 617–8555, Japan*
[6]*Application Laboratory, X-ray Division, Bruker Japan K.K., Yokohama, Kanagawa 221–0022, Japan*

(Received 16 July 2021; accepted 19 November 2021; published 16 December 2021)

The ferroaxial order, which is characterized by a rotational structural distortion in a crystal, has been recently proposed as one of ferroic orders. Though the domain formation is a characteristic feature in ferroic materials, there has been little study done concerning that for the ferroaxial order. Here, we investigate ferroaxial domains that are formed through a ferroaxial transition in two representative ferroaxial materials, $NiTiO_3$ and $RbFe(MoO_4)_2$. We spatially resolve their domain structures using an optical method based on electric-field-induced optical rotation, that is, electrogyration (EG). In $NiTiO_3$, multidomains are constructed when crystals undergo a ferroaxial transition and the domain size depends on the cooling rate around the transition temperature. Furthermore, the ferroaxial domain structure obtained by the EG measurement is well matched with that by scanning x-ray diffraction. $RbFe(MoO_4)_2$ also exhibits multidomain states in which domain patterns are different each time a crystal undergoes a ferroaxial transition. In addition, the temperature dependence of the EG signal well obeys that of the order parameter of a first-order phase transition. These results ensure the effectiveness of the EG effect to elucidate the nature of ferroaxial order.

DOI: 10.1103/PhysRevMaterials.5.124409

I. INTRODUCTION

Ferroaxial order [1,2] (or sometimes called ferrorotational order [3,4]) is a structural order in a crystal characterized by a spontaneous rotational distortion that corresponds to a vortexlike arrangement of electric dipoles. The order parameter characterizing the ferroaxial order is a ferroaxial moment $\mathbf{A}$ which is defined as $\mathbf{A} \propto \Sigma_i \mathbf{r}_i \times \mathbf{p}_i$ [3,5]. Here, $\mathbf{r}_i$ denotes a position vector of an electric dipole $\mathbf{p}_i$ at i site from a symmetrical center of the rotation. Unlike other conventional ferroic orders such as ferromagnetic and ferroelectric orders, ferroaxial order preserves both time-reversal and space-inversion symmetries. The characteristic symmetry breaking of ferroaxial order is a mirror symmetry, whose mirror plane includes the rotation axis. Note that a mirror symmetry whose mirror plane is perpendicular to the rotation axis is not necessarily broken, which is different from chirality. Despite its high symmetry, ferroaxial order is closely related to various phenomena including magnetoelectric couplings in multiferroics [1,6,7], polar vortices in nanostructured materials [5,8], and an emergence of chirality [9]. Moreover, very recently, it is suggested that when a magnetic or an electric field perpendicular to $\mathbf{A}$ is applied in ferroaxial materials, a magnetization or polarization can be induced perpendicular to both the $\mathbf{A}$ and applied fields [10]. Thus, materials showing ferroaxial order will provide opportunities to investigate new functionalities and unconventional physical phenomena.

As in other ferroic orders, the ferroaxial order is characterized by a transition from nonferroaxial into ferroaxial phases, i.e., ferroaxial transition [2]. When a crystal undergoes the ferroaxial transition, ferroaxial domains with the opposite signs of $\mathbf{A}$ will be formed. In 2020, the presence of domains was experimentally confirmed by Jin and coworkers in $RbFe(MoO_4)_2$, that is one of the representative ferroaxial materials, by using rotational anisotropy second harmonic generation [4]. They also showed the temperature variation of the areal ratio of ferroaxial domains. Furthermore, in the same year, Hayashida and coworkers succeeded in visualizing spatial distribution of ferroaxial domains in another ferroaxial material $NiTiO_3$ by using an optical method based on the electrogyration (EG) effect and by scanning transmission electron microscopy combined with convergent-beam electron diffraction [11]. Both of the compounds exhibit one of the pure ferroaxial transitions (point group $\bar{3}m \rightarrow \bar{3}$), which accompany neither ferroelectric, ferroelastic, nor gyrotropic transitions [2,11,12]. Hence, these materials are suitable for the study of the intrinsic nature of the ferroaxial order. However, how the ferroaxial domains are formed upon the transition has been visualized in neither $RbFe(MoO_4)_2$ nor $NiTiO_3$.

The crystal structure of $NiTiO_3$ at temperatures above $T_c = 1560$ K is described by the corundum structure (nonferroaxial space group $R\bar{3}c$), in which Ni^{2+} and Ti^{4+} cations are randomly distributed on cation sites [13]. At T_c, orderings of Ni^{2+} and Ti^{4+} cations take place and result in a structural

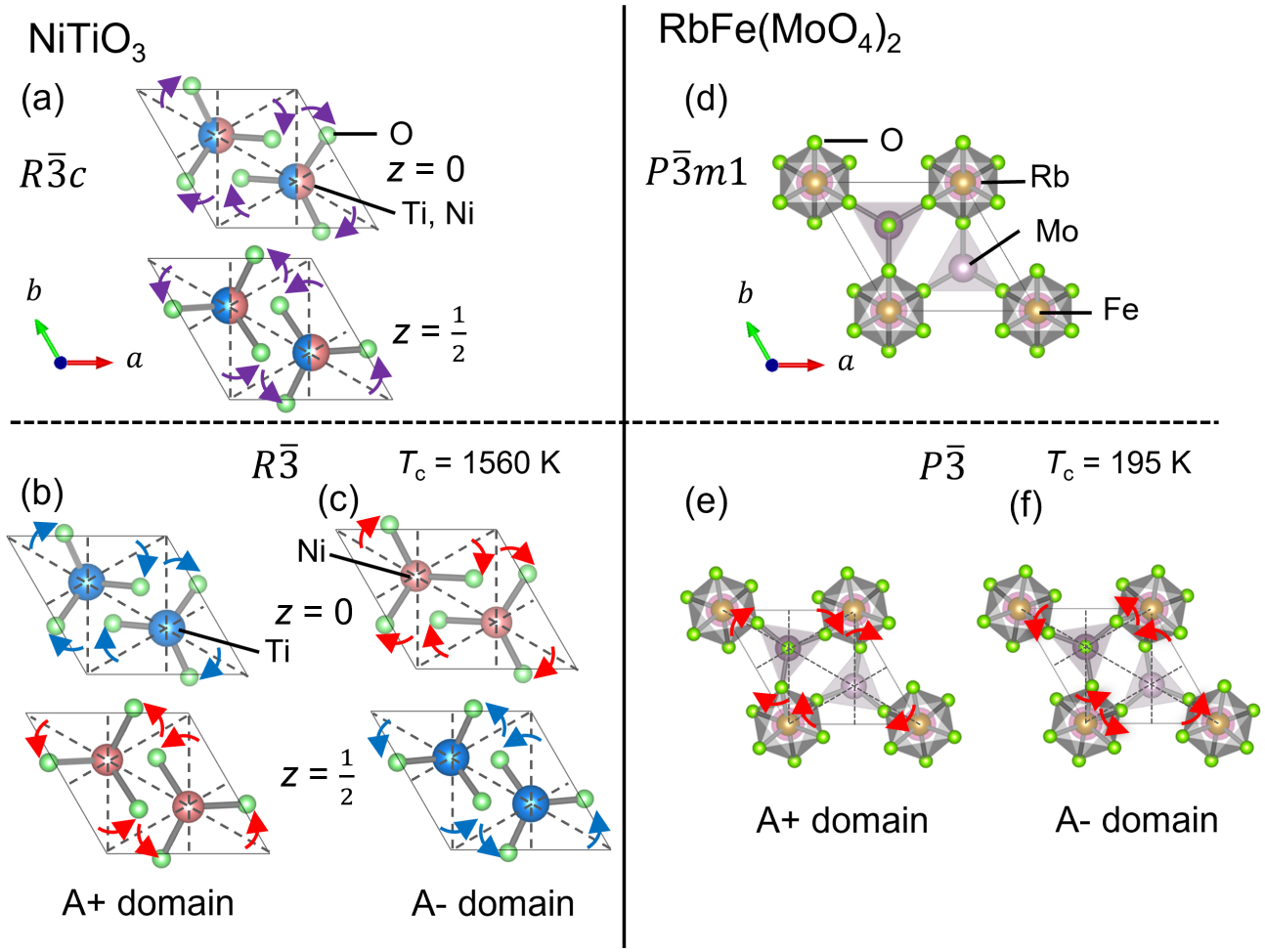

FIG. 1. Ferroaxial transitions and ferroaxial domains of $NiTiO_3$ and $RbFe(MoO_4)_2$. (a)–(c) Crystal structures of $NiTiO_3$ above (a) and below (b), (c) the ferroaxial transition temperature ($T_c = 1560$ K). Two Ti and Ni cations on $z = 0$ and $z = 1/2$ layers and six oxygen ions bonded to them are depicted. The arrows denote the direction of rotational displacements of oxygen ions from the (110)-type planes (dotted lines). The colors of arrows of purple, blue, and red in (a)–(c) correspond to the bonded cations of equally occupying Ti and Ni cations, Ti cations, and Ni cations, respectively. (d)–(f) Crystal structures of $RbFe(MoO_4)_2$ above (d) and below (e), (f) the ferroaxial transition temperature ($T_c = 195$ K). The red arrows in (e), (f) denote the direction of rotational displacements of MoO_4 tetrahedra from the high-temperature phase [the (110)-type planes (dotted lines)].

phase transition into the ilmenite structure (ferroaxial space group $R\bar{3}$). Thus, the ferroaxial transition in $NiTiO_3$ is of order-disorder type. In the low temperature phase, two domain states will be developed depending on the ordered sequence (Ni-Ti-Ni-Ti or Ti-Ni-Ti-Ni). To understand this transition and domain formation from the viewpoint of a rotational distortion, we depict two cations on $z = 0$ and $z = 1/2$ layers surrounded by respective six oxygen ions in Figs. 1(a)–1(c). In the nonferroaxial $R\bar{3}c$ phase [Fig. 1(a)], rotational distortions of oxygen ions between $z = 0$ and $z = 1/2$ layers are same in magnitude but opposite in direction (these two layers are related by the c glide operation). Thus, the rotational distortions are canceled out in a unit cell, i.e., $\mathbf{A} = \mathbf{0}$. On the other hand, in the ferroaxial $R\bar{3}$ phase, the bond length and the difference in formal charge between the oxygen ions and the cations are not the same for the two layers depending on the bonded cations Ni^{2+} or Ti^{4+}, so that rotational distortions between the two layers do not cancel out completely. Accordingly, the structure has a finite $\mathbf{A}$ in a unit cell [Figs. 1(b) and 1(c)]. Here, A+ (A−) domain is defined as the domain exhibiting the clockwise (counterclockwise) distortions of O ions bonded to Ti cations.

The crystal structure of $RbFe(MoO_4)_2$ belongs to nonferroaxial space group $P\bar{3}m1$ at room temperature. The structure is built of FeO_6 octahedra sharing their vertices with MoO_4 tetrahedra [Fig. 1(d)]. At $T_c \approx 195$ K, $RbFe(MoO_4)_2$ undergoes a structural phase transition into a ferroaxial phase (space group $P\bar{3}$), which is characterized by rotations of MoO_4 tetrahedra (or FeO_6 octahedra) about the c axis [4,14]. Thus, the rotation angle can be regarded as an order parameter of ferroaxial order and the ferroaxial transition in $RbFe(MoO_4)_2$ is of the displacive type. Depending on the directions of the rotations, two possible domain states are developed [Figs. 1(e) and 1(f)]. Here, the A+ (A−) domain is defined as the domain displaying the clockwise (counterclockwise) rotations of MoO_4 tetrahedra.

In this study, to reveal the effects of ferroaxial phase transitions on the domain formation, we examine spatial distributions of ferroaxial domains in the two representative ferroaxial materials, $NiTiO_3$ and $RbFe(MoO_4)_2$, by

utilizing the optical method based on the EG effect. We also demonstrate that scanning x-ray diffraction (XRD) can be another powerful method for visualizing ferroaxial domains. We adopt this method for $NiTiO_3$ crystals and compare the ferroaxial domain images obtained by the two methods. For $RbFe(MoO_4)_2$, we compare the temperature profile of the EG effect with that of the rotation angle of MoO_4 tetrahedra, which corresponds to the order parameter of displacive-type ferroaxial order.

II. TECHNIQUES TO OBSERVE FERROAXIAL DOMAINS

A. Electrogyration

One of the effective ways to observe ferroaxial domains is a spatial distribution measurement of the EG effect, which has been reported recently [11]. The EG effect is a phenomenon in which optical rotation is induced by an external electric field. In this study, we focus on the linear EG effect, that is, optical rotation induced linearly by an applied electric field E. In the centrosymmetric ferroaxial crystals whose point group $\bar{1}$, $2/m$, $\bar{3}$, $4/m$, or $6/m$, natural optical rotation is absent, and the rotation angle of the light polarization plane ϕ is expressed as a function of E

$$\phi = \frac{\pi d}{\lambda n}\gamma_{ijk}E_i l_j l_k = \frac{\pi}{\lambda n}\gamma_{ijk}V_i l_j l_k. \quad (1)$$

Here, d is the sample thickness, λ is the wavelength of incident light, n is the refractive index, l_j and l_k are direction cosines of the wave normal, and V $(= Ed)$ is the voltage applied to the sample (the Einstein notation is adopted). The γ_{ijk} is the third-rank axial tensor which characterizes the linear EG effect. Importantly, when the direction of light propagation and E are both parallel to a ferroaxial moment $\mathbf{A}$, the sign of tensor component γ_{333} will depend on the sign of $\mathbf{A}$ [3,11]. This means that the direction of E-induced rotation of polarization plane in A+ domain is opposite to that in A− domain. In such a situation, Eq. (1) is rewritten as

$$\phi = \frac{\pi}{\lambda n}\gamma_{333}V_3 l_3 l_3 = \frac{\pi}{\lambda n}\gamma_{333}V_3, \quad (2)$$

where $l_3 = 1$. At a fixed wavelength, ϕ is proportional to V, which is expressed as

$$\phi[\text{deg}] = \alpha[\text{deg V}^{-1}] \times V[\text{V}]. \quad (3)$$

The coefficient α $(\propto \gamma_{333})$ represents the linear EG effect, and the sign of α depends on the sign of $\mathbf{A}$. Thus, by measuring a spatial distribution of α in a ferroaxial crystal, one can obtain a two-dimensional map of ferroaxial domains. However, the magnitude of the linear EG effect is usually small $(|\alpha| \leqslant 10^{-4}\,\text{deg V}^{-1})$ [15], which makes the domain observation challenge. To overcome this problem, we adopted a field-modulation imaging technique [11,16,17] whose details will be given in the next experiment section.

B. X-ray diffraction

Scanning XRD is another way to observe a spatial distribution of ferroaxial domains. For example, A+ and A− domains in ferroaxial $NiTiO_3$ are related by the c glide operation or the twofold rotational operation about to the a axis. They are symmetry operations of the parent $R\bar{3}c$ phase but not the ferroaxial $R\bar{3}$ phase. Therefore, A+ and A− domains are crystallographically inequivalent. Thus, these two domains can be distinguished by diffraction methods if appropriate Bragg reflections are examined. In fact, twin domains, which correspond to ferroaxial domains, were observed in ilmenite-hematite solid solutions, $FeTiO_3$-Fe_2O_3, showing the same transition $R\bar{3}c \rightarrow R\bar{3}$ with $NiTiO_3$ by the electron diffraction method [18]. We calculated the crystal structure factor F of $NiTiO_3$ using a software VESTA [19] based on the room-temperature structure given in Ref. [13] and found that the reflection intensity $(\propto |F|^2)$ at $hkil = 11\bar{2}\underline{3}n$ strongly depends on the ferroaxial domain. For example, the crystal structure factor $|F_{11\bar{2}\underline{15}}|$ is 40.1 for A+ domain while 3.87 for A− domain. Therefore, by mapping reflection $11\bar{2}\underline{15}$, one can obtain spatial distributions of ferroaxial domains in $NiTiO_3$. Furthermore, the domain contrast will get reversed by mapping reflection $\bar{1}\bar{1}\underline{215}$ which is related to reflection $11\bar{2}\underline{15}$ by the mirror or the twofold rotation operation, as $|F_{\bar{1}\bar{1}\underline{215}}| = 3.87$ for A+ domain and $|F_{11\bar{2}\underline{15}}| = 40.1$ for the A− domain. This scanning-XRD-based method will obtain domain structures around the sample surface, whereas the EG-based method will obtain those averaged along the sample thickness direction. In that sense, these two methods are complementary to each other.

III. EXPERIMENT

A. Sample preparation

Single crystals of $NiTiO_3$ were grown by the flux method [20]. Powders of NiO, TiO_2, PbO, and V_2O_5 were weighted to the mass ratio 5.6:6:103:45, respectively, mixed, and well-grounded. The resulting chemicals were put into a platinum crucible with a tightly fitting lid and heated at 1623 K for 6 h and then slowly cooled to 1223 K at a cooing rate of 1 K/h in air. Plate-shaped dark brown single crystals with typical dimensions of $3 \times 3 \times 0.1\,\text{mm}^3$ were obtained and confirmed to be ilmenite-type $NiTiO_3$ by measurements of XRD and scanning electron microscope-energy dispersive x-ray analysis (SEM-EDX). In addition to the as-grown crystals, we prepared two types of annealed samples: rapidly cooled and slowly cooled samples which were obtained by annealing the as-grown crystals in air from 1623 K to a temperature below T_c at a cooling rate of 275 and 1 K/h, respectively. Note that ferroaxial domains reported in Ref. [11] were obtained for a crystal grown by the floating zone method. Thus, the growth condition of the crystals used in this study is different from that in Ref. [11].

Both polycrystalline and single-crystal samples of $RbFe(MoO_4)_2$ were prepared for measurements of neutron diffraction and EG, respectively. Polycrystalline powder samples were synthesized by the solid-state reaction [21]. First, a mixture of Fe_2O_3 and MoO_3 in the molar ratio 1:3 and a mixture of Rb_2CO_3 and MoO_3 in the molar ratio 1:1 were heated at 923 K for 24 h in air and obtained powders of $Fe_2(MoO_4)_3$ and Rb_2MoO_4, respectively. Subsequently, these powders were mixed in the molar ratio 1:1 and heated at 923 K for 24 h in air, and polycrystalline $RbFe(MoO_4)_2$ was obtained. Single crystals of $RbFe(MoO_4)_2$ were grown by the flux method [14]. Powders of Rb_2CO_3, Fe_2O_3, and MoO_3

were weighted to the molar ratio 2:1:6, mixed, well-grounded, and put into a platinum crucible with a lid. The chemicals were heated at 1073 K for 40 h in air, cooled to 773 K at a cooling rate of 2 K/h, and then to room temperature at a rate of 5 K/h. Plate-shaped transparent yellowish single crystals with typical dimensions of $2 \times 2 \times 0.2\,\mathrm{mm}^3$ were obtained and confirmed to be the $RbFe(MoO_4)_2$ structure by XRD measurements.

The widest faces of the obtained plate-shaped crystals for both $NiTiO_3$ and $RbFe(MoO_4)_2$ were perpendicular to the c axis (hexagonal setting). For our EG measurements, a pair of the widest faces of each sample were polished with pieces of abrasive paper and diamond abrasives down to the thickness of about 50 μm along the c axis. To form transparent electrodes for applying an electric field parallel to the c axis, indium/tin oxide (ITO) was sputtered to the widest faces.

B. Electrogyration measurement

Two-dimensional maps of EG on $NiTiO_3$ and $RbFe(MoO_4)_2$ were obtained using a polarized microscope by applying a field-modulation imaging technique [11,16,17]. Figure 2(a) shows a schematic illustration of the optical setup. In this technique, transmission microscope images are captured by a scientific CMOS camera (pco. edge 5.5) while a square-wave voltage is applied to a sample [the inset of Fig. 2(a)]. Then, the difference in transmitted light intensities between under the positive $(+V)$ and negative $(-V)$ voltages (ΔT) divided by the average of them (T) are calculated for each pixel of the camera. This procedure gives the spatial distribution of $\Delta T/T$. The spatial resolution of the imaging system is a few micrometers. When the angle between a polarizer and an analyzer (θ) is set at $\theta = \pm 45$ deg, $\Delta T/T$ is proportional to the rotation angle of the light polarization plane ϕ under the approximation that ϕ is small enough, which is expressed as [11]

$$\frac{\Delta T}{T} \cong \pm 4\frac{\pi}{180}\phi = \pm 4\frac{\pi}{180}\alpha V. \tag{4}$$

Since the sign of α depends on that of **A**, spatial distributions of $\Delta T/T$ will correspond to those of ferroaxial domains. As mentioned in Sec. II, however, the magnitude of α is usually small, and therefore that of $\Delta T/T$ is also small. To obtain two-dimensional maps of such small signals of $\Delta T/T$ with suppressing noises, we captured large amounts (15 000 $\sim$ 20 000) of $\Delta T/T$ maps for each measurement, which were then averaged. By this field-modulation imaging technique, a $\Delta T/T$ signal of the order of 10^{-5} can be detected.

When a finite $\Delta T/T$ signal is induced by the EG, not by other effects such as E-induced optical birefringence and absorption, the sign of $\Delta T/T$, and hence the domain contrast, will be reversed between the polarization angles of $\theta = +45$ deg and -45 deg. Thus, to confirm that the contrast originates definitely from the EG, we examined such a contrast reversal, the results of which are given in Supplemental Material Figs. S1 and S2 [22]. The domain images shown in the main text of this paper are taken in the configuration of $\theta = +45$ deg.

C. X-ray diffraction measurement

To observe ferroaxial domains in $NiTiO_3$, scanning XRD measurements in a slowly cooled sample were performed at room temperature by using a multipurpose x-ray diffractometer (Bruker AXS GmbH, D8 DISCOVER). Cu Kα radiation was used for an incident x-ray beam which was collimated with 50 μm diameter pinhole. The sample was mounted on the diffractometer so that the c plane (parallel to the sample surface) was parallel to the XY stage of the diffractometer. For the ferroaxial domain mapping, sample-position profiles of reflection intensities at $11\bar{2}\underline{15}$ and $\bar{1}\bar{1}2\underline{15}$ were detected while translating the sample position with $\underline{25}$ μm step size. We chose the diffraction geometry close to the orthogonal incidence (the angle between the incident x-ray beam and the sample surface was about 83 deg). This means that the spatial resolution of our scanning XRD measurements is nearly the beam size.

Besides the scanning XRD measurements, we also examined a possible application of XRD topography with the Berg-Barrett technique [23,24] to the observation of ferroaxial domains. This technique is widely used for the visualization of defects (e.g., dislocations, twins, and domain walls) in crystalline samples. Since the quality of the images obtained by our XRD topography measurements was not as good as that of scanning XRD, we show the results of XRD topography only in Supplemental Material Fig. S3.

D. Neutron diffraction measurement

In $RbFe(MoO_4)_2$, the rotation of MoO_4 tetrahedra will behave as an order parameter. Although there are some reports on the crystal structure of $RbFe(MoO_4)_2$ [14,21], the temperature dependence of the rotation have not been provided. Thus, we investigated it by the powder neutron diffraction method. Neutron diffraction measurements were performed on a polycrystalline sample of $RbFe(MoO_4)_2$ using a high resolution powder diffractometer (BL08, SuperHRPD) at MLF of J-PARC [25]. The high resolution up to $\Delta d/d = 0.035\%$ allows us to distinguish a lot of Bragg reflections, which is essential for accurate estimates of magnitudes of the rotational distortion. The measurements were done across T_c from 210 to 100 K during cooling the sample, and the Rietveld refinements of the obtained data were carried out using Z-Rietveld software [26,27]. The details of the refinements (Tables S1, S2 and Fig. S4) and the temperature profiles of the refined lattice constants (Fig. S5) are given in the Supplemental Material [22].

IV. RESULTS AND DISCUSSION

A. Annealing condition dependence of ferroaxial domains in $NiTiO_3$

Figure 2 summarizes the optical images [Figs. 2(b)–2(e)] and spatial distributions of $\Delta T/T$ [Figs. 2(f)–2(i)] in the three different types of $NiTiO_3$: as-grown, rapidly cooled, and slowly cooled samples. In these EG measurements, the directions of light propagation and an applied electric field were both parallel to the c axis, and EG corresponding to the γ_{333} component was probed. The wavelength of incident light was 660 nm, and applied voltages were ± 100 V. The

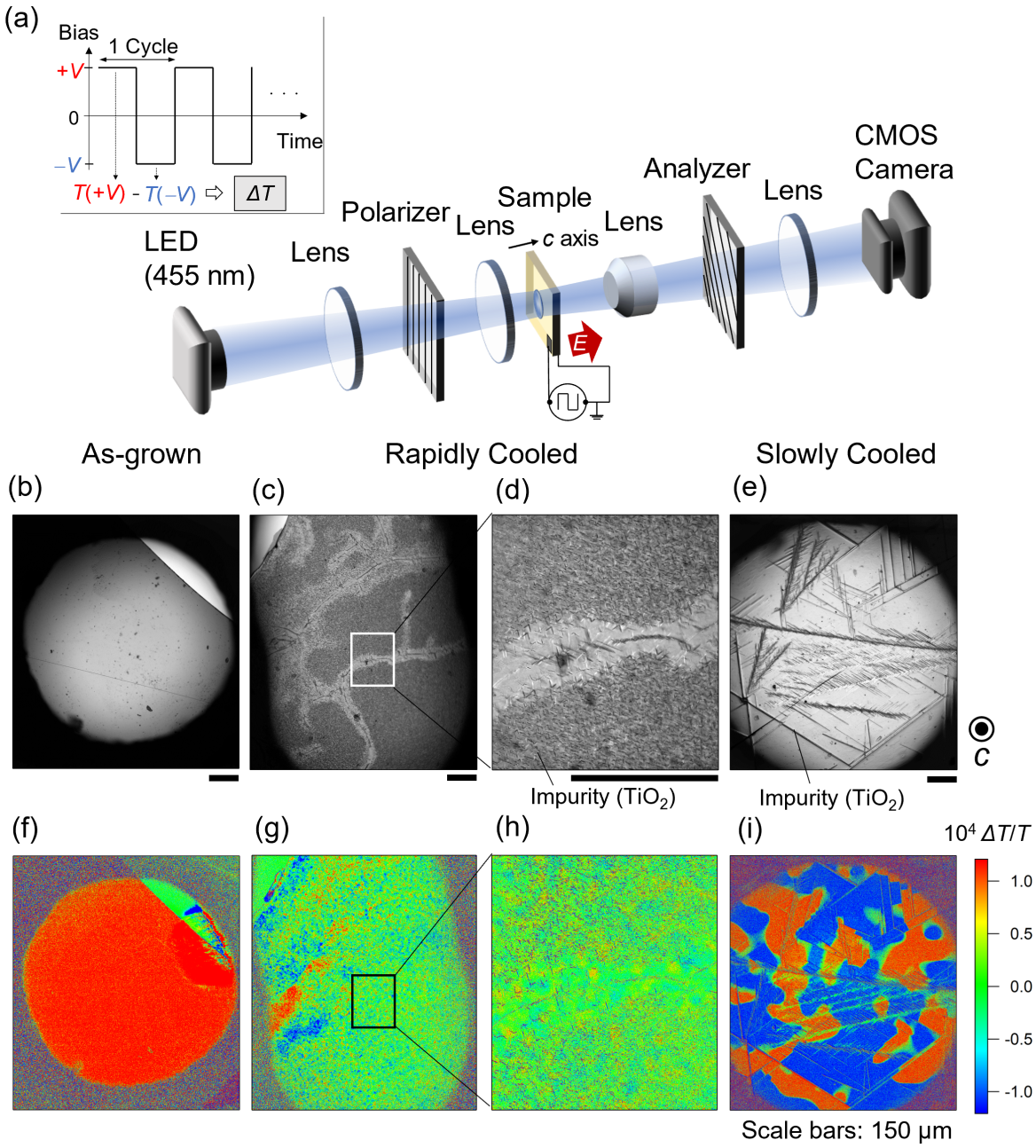

FIG. 2. Spatial distributions of ferroaxial domains observed by using electrogyration in $NiTiO_3$. (a) Optical setup of EG measurement using a field-modulation imaging technique. The inset shows temporal evolution of applied voltages V during the measurement. (b)–(e) Transmission optical microscopy images of (b) as-grown, (c), (d) rapidly cooled, and (e) slowly cooled samples with the incidence of light along the c axis (scale bars: 150 μm). Bright areas [right upper part of (b) and left upper part of (c)] correspond to blank areas. The image of (d) shows an enlarged view of a part of panel (c). Dark areas in the annealed samples (c)–(e) correspond to impurities of TiO_2. (f)–(i) Two-dimensional maps of $\Delta T/T$, which corresponds to EG, at the same area as panels (b)–(e), respectively.

measurements were performed at room temperature in the ferroaxial phase. As shown in Fig. 2(f), the $\Delta T/T$ map of the as-grown sample shows a monotonous contrast of red, suggesting that the directions of E-induced rotation of polarization plane, i.e., the signs of α, are the same in the whole observation area. Therefore, the as-grown sample consists of a single ferroaxial domain, at least in the observation area. On the other hand, the $\Delta T/T$ maps of the annealed samples exhibit both contrasts of red and blue, suggesting that they consist of multiferroaxial domains, namely, A+ and A− domains [see Figs. 2(g)–2(i)]. Note that in the optical images of the annealed samples [Figs. 2(c)–2(e)], dark inclusions are seen, which were identified as TiO_2 impurities by SEM-EDX (see Supplemental Material Fig. S6 [22]). Tiny TiO_2 impurities are dense almost all over the rapidly cooled sample [Figs. 2(c) and 2(d)], whereas large line-shaped impurities are sparsely located in the slowly cooled sample [Fig. 2(e)]. Because these impurities are not observed in the as-grown

sample [Fig. 2(b)], they are produced by the annealing process, most likely due to an interaction between the sample surfaces and oxygen at high temperature [28].

Next let us mention the domain sizes of the annealed samples. In the rapidly cooled sample, large domains are found in several areas [see middle-left side of Fig. 2(g)]. However, it mainly consists of tiny domains whose sizes are on the order of micrometers or the regions with weak $\Delta T/T$ signals [green regions of Fig. 2(h)]. The green regions in the rapidly cooled sample are likely to correspond to the areas in which A+ and A− domains coexist in the length scale below the resolution limit of the measurement system. By contrast, the slowly cooled sample consists of larger domains whose sizes are several hundreds of micrometers [Fig. 2(i)]. The magnitude of EG in the single domain areas was found to be almost the same in all the samples, which gives $\alpha \approx 2 \times 10^{-5}$ [deg V^{-1}]. This value is consistent with that of a sample grown by the floating zone method [11].

The as-grown sample consists of a single domain. This is probably because it crystallized at a temperature below T_c during the flux growth and has never undergone the ferroaxial phase transition. By contrast, the annealed samples consist of multidomains, indicating that the multidomain state is formed upon the ferroaxial transition at T_c during the annealing procedure. Furthermore, the domain sizes of the slowly cooled sample are much larger than those of the rapidly cooled sample, which suggests that slower cooling speed, especially around T_c, makes a domain size larger. This relationship between the cooling speed and domain size is reasonable by considering that slow cooling around T_c promotes the nucleus growth of each domain. The similar relationship between the cooling speed and domain size has been observed in the ilmenite/hematite solid solutions [18]. Also, in the annealed samples, not all but some of the TiO_2 impurities are clamped to the domain boundaries [compare Fig. 2(e) with 2(i)]. The density of those impurities are much larger in the rapidly cooled than in the slowly cooled samples [compare Figs. 2(c) and 2(d) with 2(e)], which may also affect the formation of domains and the domain size.

B. Comparison of electrogyration and x-ray diffraction images in $NiTiO_3$

Considering the structure-property relationship between ferroaxial order and EG in terms of the symmetry, the $\Delta T/T$ maps shown in Fig. 2 will reflect ferroaxial domains [11]. However, there has been no study which provides direct comparison between the sign of EG and that of rotational structural distortion characterizing the ferroaxial order. In this subsection, we compare a $\Delta T/T$ map obtained by EG and reflection-intensity maps by scanning XRD. For this comparison, we prepared a slowly cooled sample. This is because the domain size of slowly cooled samples is the order of $10^2 \sim 10^3$ μm [Fig. 2(i)], which is larger than the spatial resolution of the x-ray diffractometer used in this study (see Sec. IIIC). Figs. 3(a) and (b) show the two-dimensional intensity maps of reflections $11\bar{2}\underline{15}$ and $\bar{1}\bar{1}2\underline{15}$, respectively, obtained by scanning XRD measurements. To index these reflections (including their signs), we adopt the setting of crystal axes as shown in Fig. 3(c). In these maps, there are

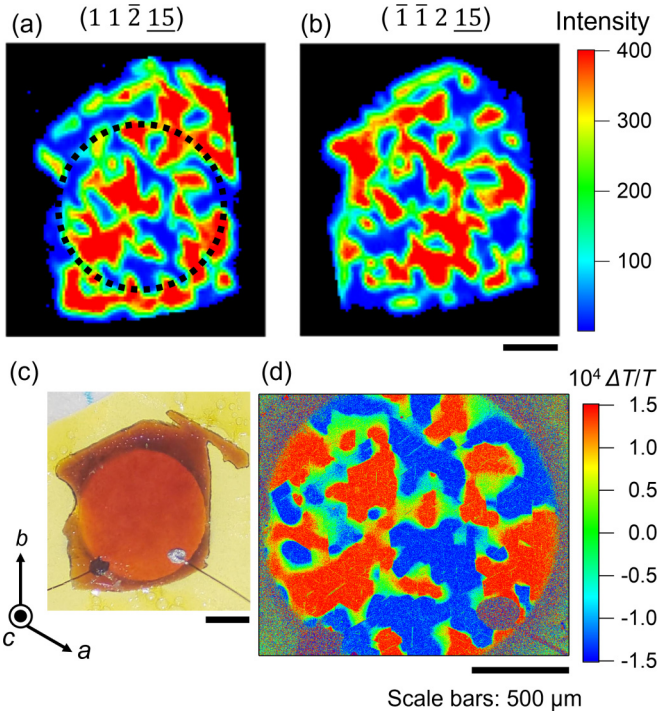

FIG. 3. Comparison of ferroaxial domains observed in a slow cooled sample of $NiTiO_3$ by x-ray diffraction (XRD) and electrogyration (EG) measurements. (a),(b) XRD results showing two-dimensional maps of diffraction intensities of reflections (a) $11\bar{2}\underline{15}$ and (b) $\bar{1}\bar{1}2\underline{15}$. The color contrasts of (a) and (b) are reversed with each other. (c) A photograph of the sample prepared for the EG measurement. (d) EG result showing a two-dimensional map of $\Delta T/T$. The dotted circle in panel (a) corresponds to the EG observation area of panel (d) [a hole on the substrate in panel (c)]. Scale bars: 500 μm. Red and blue areas in panels (a), (d) are well matched with each other and correspond to either A+ or A− domains.

both red (high intensity) and blue (low intensity) areas, and the contrasts are reversed between the two maps [compare Fig. 3(a) with 3(b)]. Considering the difference in the crystal structure factors between A+ and A− domains (see Sec. II B), the observed contrasts correspond to ferroaxial domains.

To compare domains observed by XRD with that by EG, we performed the EG measurements on the same sample used for the abovementioned XRD measurements. For sufficient light intensity and an application of voltage, the surface opposed to that was used for the XRD measurements was polished down to the thickness of 33 μm, and ITO was sputtered to both surfaces [Fig. 3(c)]. This EG measurement was performed in the same settings described in Sec. IV A, except that the wavelength of incident light was 625 nm. Figure 3(d) shows the obtained spatial distribution of $\Delta T/T$, which corresponds to the map of EG. In most of the regions, the observed contrast is well matched with that observed by the XRD mapping measurements [compare Fig. 3(d) with the area surrounded by the dotted circle in Fig. 3(a)]. This matching between the domains observed by the two different methods complementarily supports their effectiveness for the observation of ferroaxial domains. In addition, whereas the XRD maps reflect domain structures near the surface, the EG maps show the domains averaged in the thickness direction.

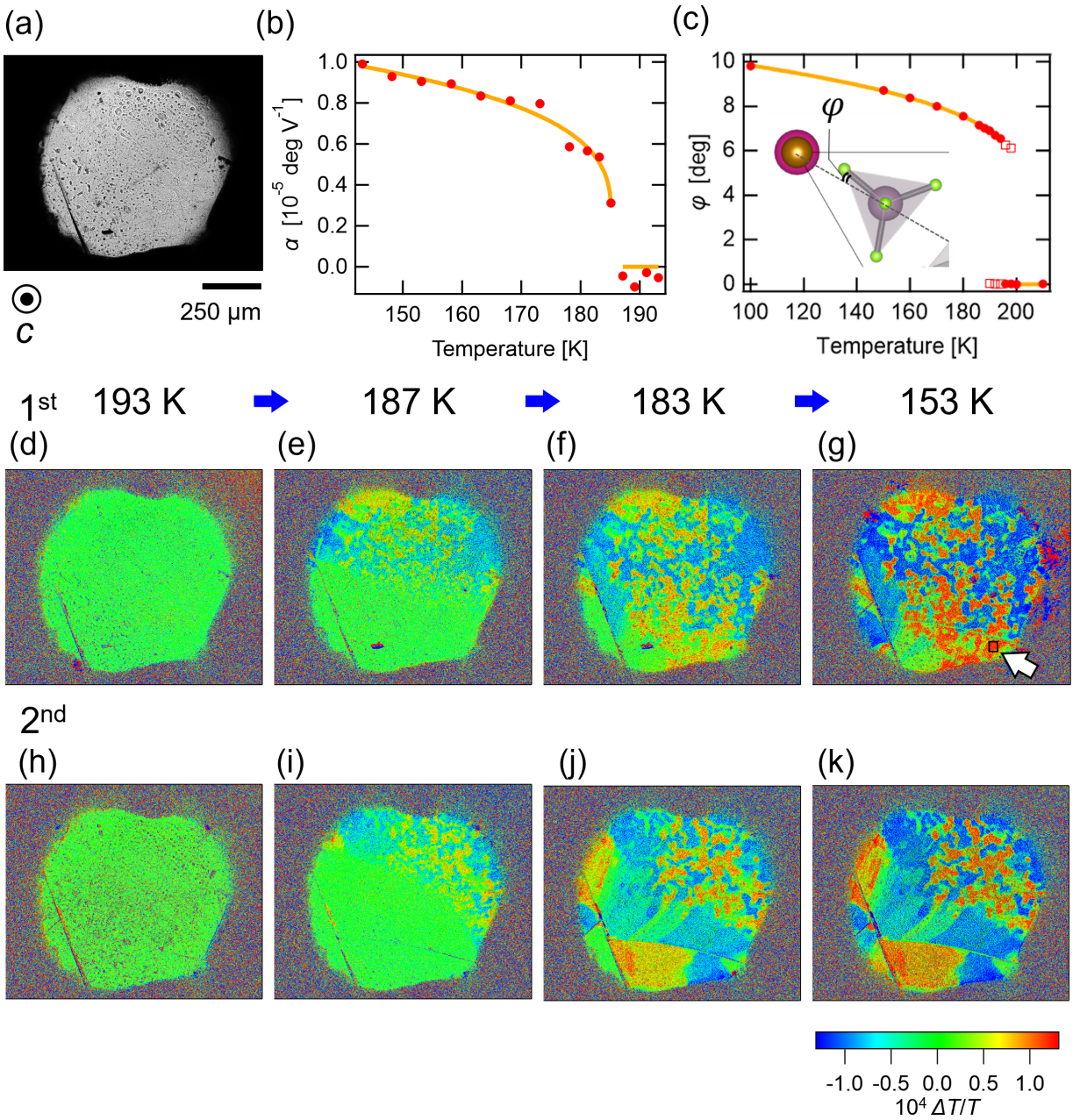

FIG. 4. Temperature evolution of ferroaxial order in $RbFe(MoO_4)_2$. (a) Transmission optical microscopy image with the incidence of light along the c axis (scale bar: 250 μm). (b) Temperature dependence of the magnitude of EG at the single domain area denoted by a black box pointed by a white arrowhead in panel (g). The orange curve is the fitting by the function of the order parameter in the first-order phase transition given in Eq. (5). (c) Temperature dependence of the rotation angle of the MoO_4 tetrahedra obtained by the Rietveld refinements of the neutron diffraction data. The rotation angles of the minority phase are denoted by open squares. The orange curve is the fitting by the function given in Eq. (5). The inset shows the definition of the angle φ. (d)–(k) Two-dimensional maps of $\Delta T/T$ obtained at various temperatures in the same area as panel (a). The first column (d)–(g) and the second column (h)–(k) show the results obtained during the first and the second cooling of the sample, respectively.

This suggests that the ferroaxial domains in this sample are almost uniform (single domain) in its thickness direction ($\| c$).

C. Temperature evolution of ferroaxial domains in $RbFe(MoO_4)_2$

In $NiTiO_3$, T_c (=1560 K) is too high to examine the evolution of domains upon its ferroaxial phase transition. By contrast, T_c (= 195 K) of $RbFe(MoO_4)_2$ is accessible by using a conventional cryostat. Thus, to examine the evolution of domain formation upon a ferroaxial transition, we measured temperature dependence of $\Delta T/T$ maps, that is, spatial distributions of EG in $RbFe(MoO_4)_2$ over a wide temperature range. Figures 4(d)–4(k) show spatial distributions of the EG effect in $RbFe(MoO_4)_2$ obtained at selected temperatures. The experimental setup was the same with that for measurements on $NiTiO_3$ except for the wavelength of incident light (λ = 455 nm) and applied voltages ($V = \pm 200$ V). The cooling

sequence was repeated twice, and the results upon the first and the second cooling runs are displayed in Figs. 4(d)–4(g) and Figs. 4(h)–4(k), respectively. The cooling rate around T_c was 0.1 K/min. Here, a 3 × 3 median filter was applied to the raw images of $\Delta T/T$ maps to suppress noises. Above the transition temperature in the nonferroaxial phase ($P\bar{3}m1$), the $\Delta T/T$ maps show a monotonous and weak (green) contrast as shown in Figs. 4(d) and 4(h). This is because the EG effect corresponding to the γ_{333} component is symmetrically forbidden in the nonferroaxial phase. With lowering sample temperature, contrasts of red and blue corresponding to opposite directions of EG start to grow from the upper side in the images [Figs. 4(e) and 4(i)]. These red and blue regions correspond to either A+ or A− domains, which suggests that the sample undergoes the ferroaxial transition at 187 K. Then, at 183 K, the contrasts spread almost all over the sample [Figs. 4(f) and 4(j)] and get stronger with further decreasing temperature [Figs. 4(g) and 4(k)]. It is noteworthy that the domain structures obtained during the first and the second cooling are completely different [e.g., compare Fig. 4(g) with 4(k)]. This suggests that the ferroaxial domains were reconstructed by undergoing the transition. In both the results, various sizes of domains with the orders of $10^1 \sim 10^2$ μm are seen. In addition, there are broad green areas corresponding to weak EG signals, which suggests that there are opposite domains along the thickness directions and/or domains whose sizes are much smaller than the spatial resolution of the imaging system (a few micrometers). In Ref. [4], it was reported that the ferroaxial domain size of $RbFe(MoO_4)_2$ is less than 50 μm in diameter, and our results do not contradict it. It was also reported in Ref. [4] that the ratio of A+ and A− domains in the observation area (50 μm in diameter) gradually changed with decreasing temperature from just below T_c to 130 K. In our measurements, although we observed gradual growth of domains most likely due to thermal conduction, we did not observe a motion of domains with decreasing temperature.

In Fig. 4(b), we show the temperature dependence of the magnitude of EG (α[deg V^{-1}]) in the first cooling. The α at each temperature was calculated from the averages of $\Delta T/T$ in the pixels at a selected single ferroaxial domain area denoted by a black box in Fig. 4(g). In Fig. 4(c), we also plot the temperature dependence of the rotation angle φ of the MoO_4 tetrahedra obtained by the Rietveld refinements of the neutron diffraction data. Here, φ is taken as the displacement angle from the [$\bar{1}$100] axis [see the inset of Fig. 4(c)]. In the temperature range from 198 to 190 K, the high temperature $P\bar{3}m1$ phase and the low temperature $P\bar{3}$ phase are found to coexist and, thus, the rotation angles for the minority phase are shown as open squares in Fig. 4(c) [see also Supplemental Material [22]]. The temperature profiles of α and φ are similar to each other, though they show different behaviors around T_c. This is most likely because α just below T_c will reflect the averaged magnitude of EG of the coexisting high temperature and low temperature phases. The temperature profiles of α and φ are fitted by the function of

$$\alpha(T),\ \varphi(T) = \begin{cases} 0, & T > T_c \\ \sqrt{a + b\sqrt{T_d - T}}, & T \leqslant T_c \end{cases}, \qquad (5)$$

which characterizes the first-order phase transition [4,29,30]. Here, a, b, and T_d are the fitting parameters, where $T_d = T_c + \frac{a^2}{b^2}$. The fitting yields $T_c = 185.5 \pm 0.5$ K for $\alpha(T)$ and $T_c = 190 \pm 3$ K for $\varphi(T)$, which are consistent with the previously reported values of $T_c (= 190 \sim 195$ K) [4,14]. The slight difference in the value obtained from the EG measurement is probably due to a poor thermal contact between the sample and the cold stage. The success of the fitting clearly shows that the rotation angle of the MoO_4 tetrahedra behaves as the order parameter, and one can also deduce the order parameter of ferroaxial order from $\Delta T/T$ maps, that is, spatial distributions of EG.

Besides the temperature dependence of EG, we also measured the wavelength dependence. Figures 5(a)–5(d) show the $\Delta T/T$ maps obtained with four different wavelengths of incident light at 148 K in the second cooling. As seen in these figures, the EG signals, and hence the domain contrasts, are stronger for shorter wavelength. Figure 5(e) shows the wavelength dependence of the magnitude of EG calculated from the averages of $\Delta T/T$ in the pixels at a single ferroaxial domain area denoted by a white box in Fig. 5(a). The dispersion feature of EG is similar to that in a transparent lead tungstate crystal [31]. $RbFe(MoO_4)_2$ crystals are almost transparent in visible light regions and show an absorption peak originating from defects at around 450 nm [32]. However, no anomaly corresponding to the absorption peak was observed in the dispersion of EG in our wavelength resolution.

V. SUMMARY

In summary, the effect of ferroaxial phase transition on the domain formation in $NiTiO_3$ and $RbFe(MoO_4)_2$ was examined by using the electrogyration (EG) effect. In $NiTiO_3$, by comparing the domains in as-grown and annealed samples, we found that the multidomains are formed in samples which undergo the ferroaxial transition and that the domain size tends to grow with lowering a cooling rate at around transition temperature T_c. In addition, we confirmed that the observed spatial distributions of EG is nothing other than ferroaxial domains by comparing the results of EG and scanning x-ray diffraction (XRD) on the same sample. In other words, scanning XRD measurements is another way to visualize ferroaxial domains. In $RbFe(MoO_4)_2$, we performed EG measurements over a wide temperature range across T_c and confirmed that ferroaxial domains were formed below T_c. Furthermore, the temperature evolution of the rotation angle of the MoO_4 tetrahedra was identified from powder neutron diffraction measurements. The temperature profiles of EG and the rotation angle of the MoO_4 tetrahedra were similar and well fitted by the function of the order parameter in the first-order transition, which confirms the effectiveness of EG measurements to observe the evolution of ferroaxial order.

In the present study, we revealed the effect of the ferroaxial transition on the domain state, that is, how ferroaxial domains are formed through the transition. Furthermore, we demonstrated that electrogyration measurements allow us to directly and qualitatively extract the ferroaxial order parameter. One of the next fundamental questions about ferroaxial order is how we manipulate the order by its conjugate fields without contributions from ferroelectric or ferroelastic orders. So far, possible conjugate fields have been theoretically proposed [2,33], and a photoinduced excitation of ferroaxial order in 1T-TaS_2

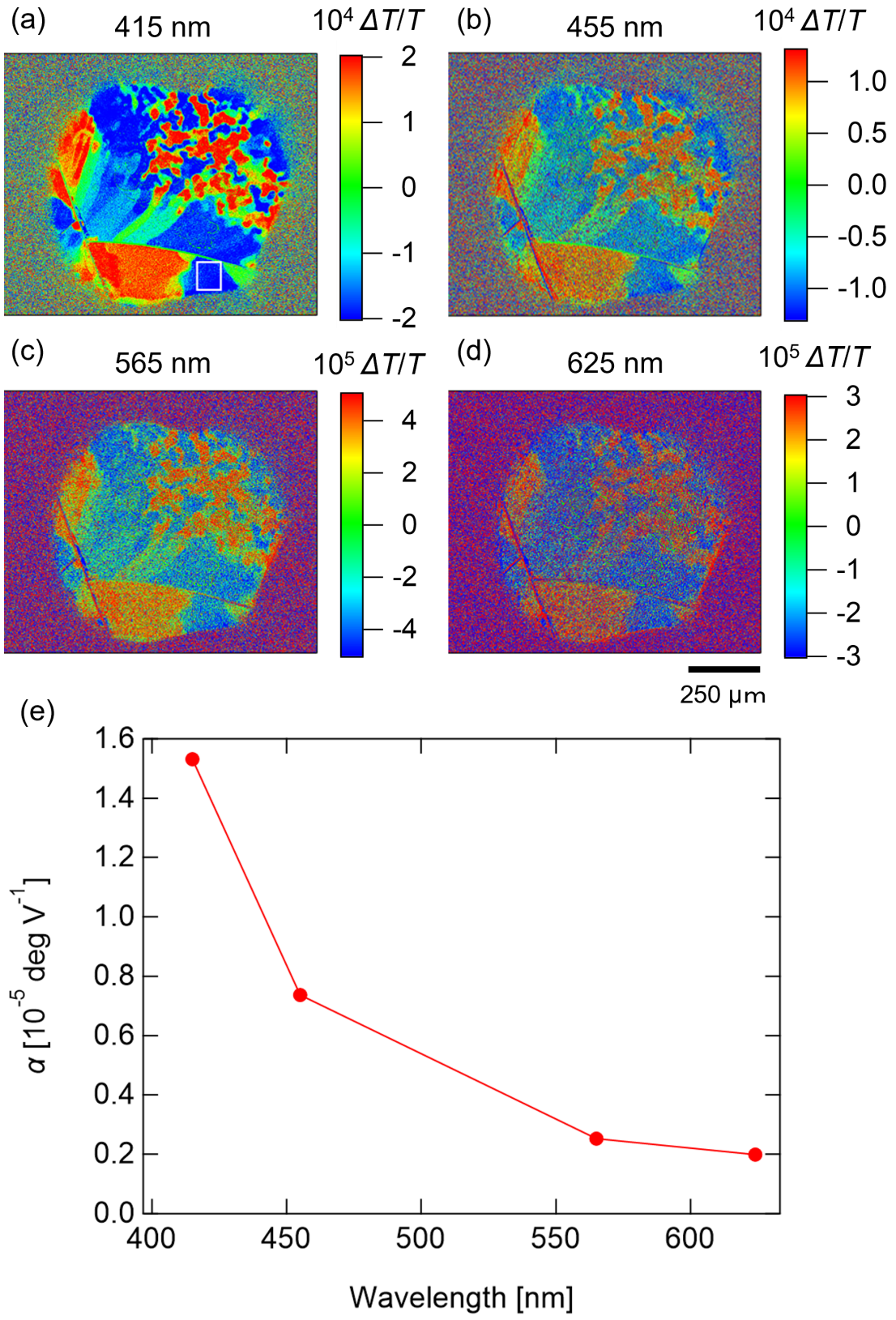

FIG. 5. Wavelength dependence of EG in $RbFe(MoO_4)_2$. (a)–(d) Two-dimensional maps of $\Delta T/T$ obtained using incident light with different wavelengths [(a) 415 nm, (b) 455 nm, (c) 565 nm, and (d) 625 nm] at the same area as Fig. 4(a). These data were obtained at 148 K during the second cooling (scale bar: 250 μm). (e) Wavelength dependence of the magnitude of EG calculated at the single domain area denoted by a white box in panel (a). The red solid line is a guide to the eye.

has been experimentally reported [34]. However, a control of the rotation, i.e., a switching of A+ and A− domains has not been experimentally achieved. Our achievements of the visualization of ferroaxial domains formed through a ferroaxial transition will be an important step toward the manipulation of domain states by applying external stimuli.

ACKNOWLEDGMENTS

We thank R. Misawa for his help with analyses of x-ray diffraction data. We also thank D. Hamane for his help with sample characterization by SEM-EDX experiments which were carried out under the Visiting Researcher's Program of the Institute for Solid State Physics, the University of Tokyo. The neutron-diffraction measurements were carried out by the project approval (J-PARC MLF Proposal No. 2019S05). The images of crystal structures were drawn using the software VESTA [19]. This work was supported by KAKENHI (Grants No. JP19H01847, No. JP19H05823, No. JP21H04988, and No. JP21H04436), the MEXT Leading Initiative for Excellent Young Researchers (LEADER), and JST CREST Grant No. JPMJCR18J2.

[1] R. D. Johnson, S. Nair, L. C. Chapon, A. Bombardi, C. Vecchini, D. Prabhakaran, A. T. Boothroyd, and P. G. Radaelli, Phys. Rev. Lett. **107**, 137205 (2011).
[2] J. Hlinka, J. Privratska, P. Ondrejkovic, and V. Janovec, Phys. Rev. Lett. **116**, 177602 (2016).
[3] S.-W. Cheong, D. Talbayev, V. Kiryukhin, and A. Saxena, npj Quantum Mater. **3**, 19 (2018).
[4] W. Jin, E. Drueke, S. Li, A. Admasu, R. Owen, M. Day, K. Sun, S.-W. Cheong, and L. Zhao, Nat. Phys. **16**, 42 (2020).
[5] S. Prosandeev, I. Ponomareva, I. Kornev, I. Naumov, and L. Bellaiche, Phys. Rev. Lett. **96**, 237601 (2006).
[6] R. D. Johnson, L. C. Chapon, D. D. Khalyavin, P. Manuel, P. G. Radaelli, and C. Martin, Phys. Rev. Lett. **108**, 067201 (2012).
[7] A. J. Hearmon, F. Fabrizi, L. C. Chapon, R. D. Johnson, D. Prabhakaran, S. V. Streltsov, P. J. Brown, and P. G. Radaelli, Phys. Rev. Lett. **108**, 237201 (2012).
[8] A. K. Yadav, C. T. Nelson, S. L. Hsu, Z. Hong, J. D. Clarkson, C. M. Schlepuëtz, A. R. Damodaran, P. Shafer, E. Arenholz, L. R. Dedon, D. Chen, A. Vishwanath, A. M. Minor, L. Q. Chen, J. F. Scott, L. W. Martin, and R. Ramesh, Nature (London) **530**, 198 (2016).
[9] T. Hayashida, K. Kimura, D. Urushihara, T. Asaka, and T. Kimura, J. Am. Chem. Soc. **143**, 3638 (2021).
[10] S.-W. Cheong, S. Lim, K. Du, and F.-T. Huang, npj Quantum Mater. **6**, 58 (2021).
[11] T. Hayashida, Y. Uemura, K. Kimura, S. Matsuoka, D. Morikawa, S. Hirose, K. Tsuda, T. Hasegawa, and T. Kimura, Nat. Commun. **11**, 4582 (2020).
[12] K. C. Erb and J. Hlinka, Phase Trans. **91**, 953 (2018).
[13] H. Boysen, F. Frey, M. Lerch, and T. Vogt, Zeitschrift Für Krist. **210**, 328 (1995).
[14] A. Waśkowska, L. Gerward, J. Staun Olsen, W. Morgenroth, M. Mączka, and K. Hermanowicz, J. Phys.: Condens. Matter **22**, 055406 (2010).
[15] O. G. Vlokh and R. O. Vlokh, Opt. Photonics News **20**, 34 (2009).
[16] Y. Uemura, S. Arai, J. Tsutsumi, S. Matsuoka, H. Yamada, R. Kumai, S. Horiuchi, A. Sawa, and T. Hasegawa, Phys. Rev. Appl. **11**, 014046 (2019).
[17] Y. Uemura, S. Matsuoka, J. Tsutsumi, S. Horiuchi, S. Arai, and T. Hasegawa, Phys. Rev. Appl. **14**, 024060 (2020).
[18] G. L. Nord, Jr. and C. A. Lawson, Am. Mineral. **74**, 160 (1989).
[19] K. Momma and F. Izumi, J. Appl. Crystallogr. **44**, 1272 (2011).
[20] G. Garton, S. H. Smith, and B. M. Wanklyn, J. Cryst. Growth **13–14**, 588 (1972).
[21] T. Inami, J. Solid State Chem. **180**, 2075 (2007).
[22] See Supplemental Material at http://link.aps.org/supplemental/10.1103/PhysRevMaterials.5.124409 for additional information on electrogyration measurements in the polarization configuration of $\theta = -45$ deg, XRD topography measurements of $NiTiO_3$, details of powder neutron diffraction analysis of $RbFe(MoO_4)_2$, and identification of impurities in $NiTiO_3$.
[23] W. F. Berg, Naturwissenschaften **19**, 391 (1931).
[24] C. S. Barrett, Trans. Metal. Soc. AIME **161**, 15 (1945).
[25] S. Torii, M. Yonemura, T. Y. S. P. Purta, J. Zhang, P. Miao, T. Muroya, R. Tomiyasu, T. Morishima, S. Sato, H. Sagehashi, Y. Noda, and T. Kamiyama, J. Phys. Soc. Jpn. **80**, SB020 (2011).
[26] R. Oishi, M. Yonemura, Y. Nishimaki, S. Torii, A. Hoshikawa, T. Ishigaki, T. Morishima, K. Mori, and T. Kamiyama, Nucl. Instrum. Methods Phys. Res. A **600**, 94 (2009).
[27] R. Oishi-Tomiyasu, M. Yonemura, and T. Morishima, J. Appl. Crystallogr. **45**, 299 (2012).
[28] H. Takei, J. Mater. Sci. **16**, 1310 (1981).
[29] A. F. Devonshire, Adv. Phys. **3**, 85 (1954).
[30] J. C. Tolédano and P. Tolédano, *The Landau Theory of Phase Transitions* (World Scientific, Singapore, 1987), Vol. 3.
[31] M. A. Novikov, A. A. Stepanov, and A. A. Khyshov, Tech. Phys. Lett. **43**, 372 (2017).
[32] R. Owen, E. Drueke, C. Albunio, A. Kaczmarek, W. Jin, D. Obeysekera, S.-W. Cheong, J. Yang, S. Cundiff, and L. Zhao, Phys. Rev. B **103**, 054104 (2021).
[33] R. E. Newnham and L. E. Cross, Mater. Res. Bull. **9**, 1021 (1974).
[34] X. Luo, D. Obeysekera, C. Won, S. H. Sung, N. Schnitzer, R. Hovden, S.-W. Cheong, J. Yang, K. Sun, and L. Zhao, Phys. Rev. Lett. **127**, 126401 (2021).